IEEE Access
Multidisciplinary ⋮ Rapid Review ⋮ Open Access Journal

Received 16 September 2022, accepted 1 October 2022, date of publication 4 October 2022,
date of current version 11 October 2022.

Digital Object Identifier 10.1109/ACCESS.2022.3211968

RESEARCH ARTICLE

Analytical Modeling of Novel High Thrust Force Density Segmented PM Consequent Pole Linear Flux Switching Machine

WASIQ ULLAH, (Graduate Student Member, IEEE), FAISAL KHAN, (Senior Member, IEEE), SHAHID HUSSAIN, (Graduate Student Member, IEEE), MUHAMMAD YOUSUF, (Graduate Student Member, IEEE), AND SIDDIQUE AKBAR
Electric Machine Design Research Laboratory, Department of Electrical and Computer Engineering, COMSATS University Islamabad, Abbottabad Campus, Abbottabad 22060, Pakistan

Corresponding author: Wasiq Ullah (wasiqullah014@gmail.com)

ABSTRACT Permanent Magnet Linear Flux Switching Machines (PMLFSMs) are potential candidates when higher thrust force (T_F) and low cost are the primal requirements. However, conventional PMLFSMs shows flux leakages and utilizes high Permanent Magnet (PM) volume (V_{PM}) that increase overall expense. Therefore, this paper proposed novel Segmented PM Consequent Pole Linear Flux Switching Machine (SPMCPLFSM) with flux bridges. In comparison with PMLFSM, the proposed SPMCPLFSM diminish detent force by $\mathbf{20.41}\%$, suppress thrust force ripples by 27.68%, reduces ripple ratio by 1.77 times, improve T_F to 2 times and boost T_F density to 2.64 times utilizing 75% PM volume and reducing PM cost by 24.16%. Moreover, to overcome computational complexity and computation time, analytical model uniting Lumped Parametric Magnetic Equivalent Circuits, vector potential and Maxwell Stress Tensor method are utilized for open circuit flux linkages, magnetic flux density, detent force and thrust force. Finally, analytical model is validated with finite element analysis (FEA) that show good agreement with FEA. Thus, authors are assured to suggest analytical techniques for early design purpose and proposed SPMCPLFSM for roller coaster application.

INDEX TERMS Analytical modelling, magnetic flux leakage, magnetic flux density distribution, permanent magnet machines, AC machines, brushless machines.

I. INTRODUCTION

Due to sophisticated gear mechanism used in rotary machine for conversion of rotational torque to translational motion, the generated linear thrust force with low efficiency and high cost. This obstacle is overcome by introducing linear motors which provide linear thrust force without any extra gear mechanism that increases reliability, provides fast dynamic response and higher overload capability. Different type of linear motors used for translational motion applications includes linear induction machine (LIM), linear permanent magnet synchronous machine (LPMSM), linear direct current machine (LDCM), and linear switched reluctance machine (LSRM).

In comparison with linear permanent magnet machines (LPMM), LPMSM show advantages of high flux density however, it's application in long stroke are limited due to high PM usage which increase overall cost [1] because LPMSM is stator surface mount PM configuration. LIM show merit of low cost however, LIM comparatively offered lower thrust force density and low efficiency. Moreover, LDCM offer simple speed control however, required high maintenance cost and low speed-force gradient. Comparatively, LSRM shows robust structure however, it has disadvantageous of low power density and higher thrust ripples [2].

To overcome the aforesaid demerits, unique features of LPMSM and LSRMs are combined to form linear flux

The associate editor coordinating the review of this manuscript and approving it for publication was Giambattista Gruosso.

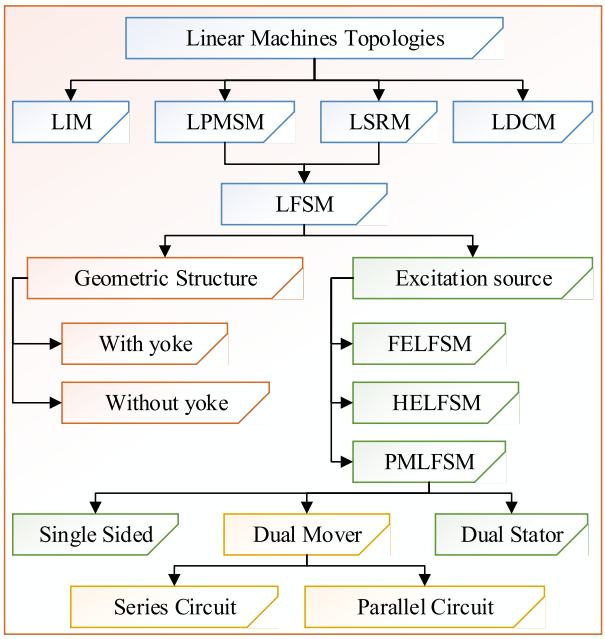

FIGURE 1. Classification of LFSMs and topologies of PMLFSM.

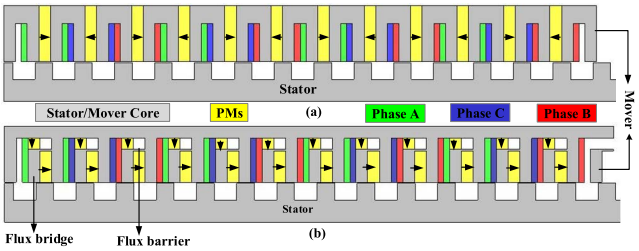

FIGURE 2. Cross sectional view (a) Conventional PMLFSM and (b) Proposed SPMCPLFSM.

TABLE 1. Coil connection and polarity of PMLFSM and SPMCPLFSM.

	Phase	PMLFSM	SPMCPLFSM
A	A1	C-D	C-D
	A2	C-D	D-C
	A3	C-D	C-D
	A4	C-D	D-C
C	C1	C-D	D-C
	C2	C-D	C-D
	C3	C-D	D-C
	C4	C-D	C-D
B	B1	C-D	C-D
	B2	C-D	D-C
	B3	C-D	C-D
	B4	C-D	D-C

switching machine (LFSM) which exhibits high-power density [3], robust secondary made of iron only (stator), applicable for long stroke application with high speed [4], bi-polar flux linkage and low manufacturing cost [5].

Based on excitation source, LFSMs are broadly classified into three categories i.e., Field excited LFSM (FELFSM), Permanent Magnet LFSM (PMLFSM) and Hybrid excited LFSM (HELFSM). FELFSM exhibits demerits of low thrust force density, HELFSM show very complex structure and PMLFSM offer higher thrust force density however, it uses excessive rare earth PM materials. With main concern in simple single sided PMLFSMs, wide range classification and different topologies are shown in Figure. 1.

For long stroke applications where high thrust force density and high efficiency are critical considerations, PMLFSM is the preferred option among linear machines. Permanent Magnets (PMs) and armature winding make up the short mover in PMLFSM's whereas passive secondary is built from lamination stack. For long stroke applications such Maglev transportation [6], rail transportation [7], subways [8], electromagnetic launch technology [9], linear propulsion technology [10], wave energy generator, and artificial heart [11], PMLFSMs is strong candidate due to passive secondary.

Comprehensive literature review indicates that state of the art PMLFSM [12] demonstrates elevated detent force, high thrust force ripples, mover flux leakages, high cost and high PM use. Author in [13] and [14] present consequent pole designed in axis-symmetric coordinates however, the developed consequent pole structure suffers from higher detent force whereas dual modulation design exhibits higher ripples content and since the PMs are positioned in rotor as well as in stator, this design highly suffers from mechanical constraints.

Due to passive stator structure, LFSMs are preferred candidate for long stroke applications. A detailed review of the LFSM for long stroke application are reported in [15]. Authors in [16] investigates segmented secondary and complementary field excited machine in dual mover form however, due to segmented secondary there is possibility of leakage flux between the segments and offers weak fault tolerant capability. This fault tolerant capability can be improved utilizing modular mover structure in dual stator form [17]. However, modular stator has mechanical constraints and offer lower thrust density. This thrust force density is improved in hybrid excited LFSM [18], however, the PMs are placed at the tip of mover tooth therefore, cooling of the PMs are complex.

Thus, to overcome abovementioned demerits, this paper introduces a novel Segmented PM Consequent Pole Linear Flux Switching Machine (SPMCPLFSM) with flux barrier and flux barrier. The proposed design has efficiently overcome leakage flux and transfer to the linkage flux utilizing adjacent flux bridges resulting reduction in detent force and thrust force ripples. Conventional PMLFSM and proposed SPMCPLFSMs are shown in Figure. 2(a) and Figure. 2(b) respectively whereas coil configuration and its polarity are listed in Table 1. Polarities of armature coils are mentioned from left to right for each four-coil set of corresponding phases in term of dot (D) and cross (C). Note that this coil connection is obtained based on coil test results.

Aforesaid categories of LFSM's are accurately model for electromagnetic performance before proceeding to manufacturing and fabrication utilizing numerical based Finite Element Analysis (FEA). When utilised for early design and performance analysis, FEA is time-consuming and computationally challenging [19]. Due to many iterations, FEA

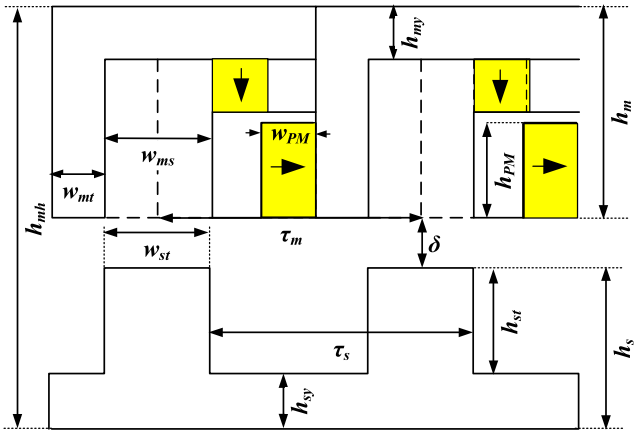

FIGURE 3. Definition of geometric design parameters.

considers geometric intricacies and necessitates costly software and technology, prolonged computations, and enormous drive memory [20].

To cope with computationally complication, computational period, computer memory and drive storing alternate analytical modelling approaches are predicted for initial design [21]. In order to develop an analytical model for flux linkages, no-load and on-load Magnetic Flux Density (MFD) distribution, Detent force, and thrust force, expressions incorporating Lumped Parametric Magnetic Equivalent Circuits (LPMEC), vector potential governed by Laplace Equations (LE), and Maxwell Stress Tensor (MST) method are used. Moreover, the JMAG Commercial FEA Package v18.1 is employed to verify the analytical model with the accompanying FEA.

The primary contribution of this study is the construction of a unique SPMCPLFSM with flux bridge and flux barriers to address the aforementioned shortcomings of the traditional PMLFSM. Additionally, the electromagnetic performance of the newly designed SPMCPLFSM is examined with that of the PMLFSM to demonstrate its notable performance. To combat computational complexity and time consumption, analytical modelling encompassing LPMEC (for validating open-circuit flux linkage), vector potential governed by LE (for validating MFD), and MST (for validating detent force and thrust force) are incorporated and confirmed with commercial FEA package.

In the following, section II present SPMCPLFSM construction, section III illustrate comparison of PMLFSM with SPMCPLFSM. Section IV illustrates analytical techniques of SPMCPLFSM, Section V analyse validation of analytical methodologies and finally some conclusions are drawn in section VI.

II. SPMCPLFSM CONSTRUCTION

Design variable of SPMCPLFSM is specified in Figure. 3 and recorded in Table 2. It is worth mentioning that design parameters are based on author previous studies in [12] with slight modification. Figure. 2(a) demonstrates that a traditional PMLFSM has a PM interposed among mover slots,

TABLE 2. Geometry parameters of SPMCPLFSM.

Parameter	Symbol	Dimension	(unit)
Stator pole pitch	τ_s	36	mmm
Mover pole pitch	τ_m	42	
Mover tooth width	w_{mt}	10.5	
Stator tooth width	w_{st}	15.75	
Mover slot width	w_{ms}	10.5	
Mover back iron height	h_{my}	15.75	
Stator back iron height	h_{sy}	20	
Magnet width	w_{PM}	10.5	
Mover height	h_m	50	
Stator height	h_s	35	
Stator tooth height	h_{st}	15	
Magnet height	h_{PM}	10.5	
Air gap length	δ	1	
Machine height	h_{mh}	86	

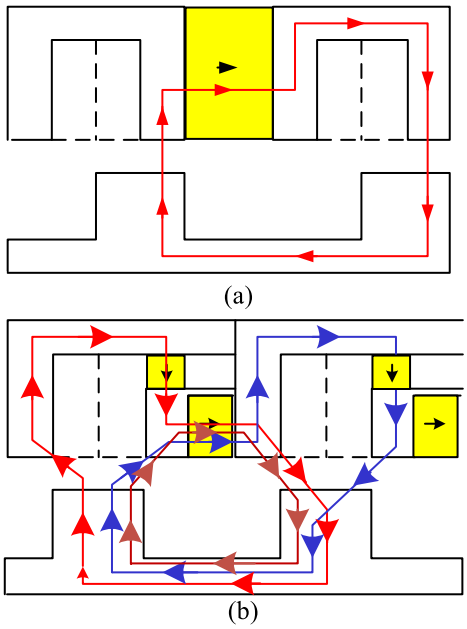

FIGURE 4. Flux modulation in (a) Conventional PMLFSM and (b) Proposed SPMCPLFSM.

whereas Figure. 2(b) illustrates a proposed SPMCPLFSM that uses Neomax segmented PMs to inhabit an H-shaped stator tooth. First segmented is placed on top of flux bridge is whereas the 2nd segmented is enclosed in flux barrier. This PM segmentation significantly contributes to improving flux modulation phenomena while decreasing overall PM usage. It is important to mention that PMLFSM uses 756000 mm3 whereas SPMCPLFSM utilizes 574560 mm3 PM volume.

It is worth mentioning that 1st PMs segment alter flux distribution that reduce flux leakages going across the mover yoke and 2nd PMs reinforce flux distribution occurring through stator slot and flux bridges as shown in Figure. 4. The circumferential PMs aid to prevent flux leakages from PM end edges in the mover, which leads to a greater magnetic flux density in the mover yoke and better flux modulation, flux distribution, and flux linkage.

Detailed flux modulation in proposed SPMCPLFSM (as shown in Figure. 4(b)) shows that for one pole pitch

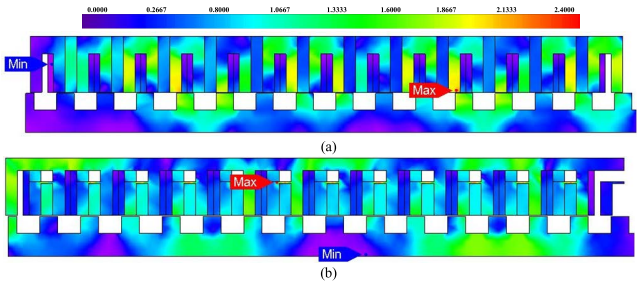

FIGURE 5. Nephogram of on-load magnetic flux density map in (a) PMLFSM and (b) SPMCPLFSM.

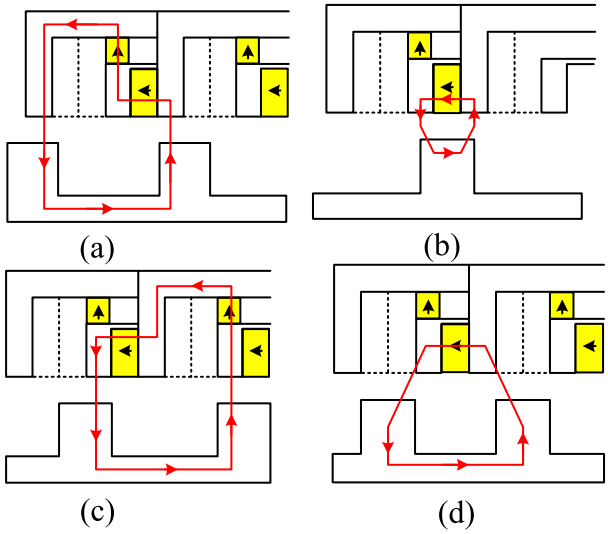

FIGURE 6. Operating principle of SPMCPLFSM (a) $\theta = 0°$ (b) $\theta = 90°$ (c) $\theta = 180°$ and (d) $\theta = 270°$.

movements, the flux linkage from stator to mover through air-gap occurs though mover back iron height as well as flux bridges. Top PMs divert the flux to the flux bridge to provide alternate path for superposition of the flux linkage directly through the flux bridge. The flux superimposes at 2nd PMs segment and link the stator through air-gap and enhance magnetic flux density as shown in Figure. 5 for load condition. This enhancement in flux modulation phenomena ultimately leads to better electromagnetic performances and results higher thrust force, diminish detent force, suppress thrust force ripples and boost thrust force density.

Operating principle of SPMCPLFSM is indicated in Figure. 6. Negative maximum flux linkage of Phase-A is achieved when relative displacement between stator and mover are shown in Figure. 6(a) assuming $\theta = 0°$. Coil Flux linkage becomes zero when $\theta = 90°$ and stator pole is aligned with PMs which provided a short circuit path as shown in Figure. 6(b). with further movement of the mover relative to stator, maximum positive flux linkage is achieved at $\theta = 180°$ as shown in Figure. 6(c). Finally, the flux linkage become zero when $\theta = 270°$ as shown in Figure. 6(d). A bi-polar flux linkage is attained when mover move from Figure. 6(a) to Figure. 6(d) with respect to stator. A typical bi-polar flux linkage over one periodic boundary is shown in Figure. 7.

TABLE 3. Quantitative Electromagnetic performance of SPMCPLFSM for various slot/pole combination.

Performance indicator (unit)	12/10	12/14	12/34	12/38
Φ_{p-p} (Wb)	1.4568	1.788	1.58732	1.438
F_d (N)	18.7321	15.8647	16.7832	17.9475
T_F (N)	144.544	154.6747	150.052	145.872
T_{F-den} (kN/m^3)	251.573	269.20	261.159	253.88

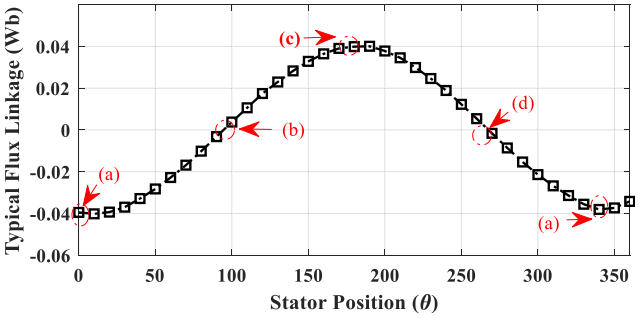

FIGURE 7. Typical flux linkage over one periodic boundary.

III. COMPARISON OF PMLFSM WITH SPMCPLFSM

To assess how effective the proposed SPMCPLFSM over PMLFSM is, a detailed comprehensive electromagnetic performance analysis with key performance indicators i.e. Open-Circuit Flux linkages (Φ_{p-p}), Detent force (F_d), thrust force (T_F), thrust force ripples (T_{F-rip}), thrust force ripple ratio (K_{rip}), thrust force density (T_{F-den}) and PM volume (V_{PM}) are carried out. Key performance indicators i.e. T_{F-rip}, K_{rip} and T_{F-den} are expressed as

$$T_{F-rip} = T_{F-max} - T_{F-min} \tag{1}$$

$$K_{rip} = \frac{T_{F-rip}}{T_F} 100\% \tag{2}$$

$$T_{F-den} = \frac{T_F}{V_{PM}} \tag{3}$$

whereas T_{F-max} is maximum thrust force and T_{F-min} is minimum thrust force.

Electromagnetic performance with the foregoing performance indicators is initially calculated for various slot/pole combination. Comparison holds for various slot/pole combination as listed in Table 3. Analysis based on key performance indicator reveals that SPMCPLFSM with 12/14 slot/pole is optimal design therefore selected for detailed investigation in the foregoing sections.

Figure 8 illustrates the open circuit flux linkages of the PMLPFSM and SPMCPLFSM. Analysis demonstrates that SPMCPLFSM design offers more symmetrical flux linkages than the traditional PMLFSM due to least end effect. In contrast to the SPMCPLFSM, which has a positive peak at 0.8453 Wb and a negative peak at −0.9435 Wb (peak to

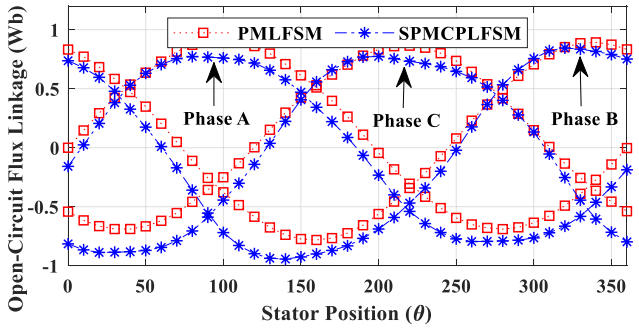

FIGURE 8. Open circuit flux linkage behavior in PMLFSM and SPMCPLFSM.

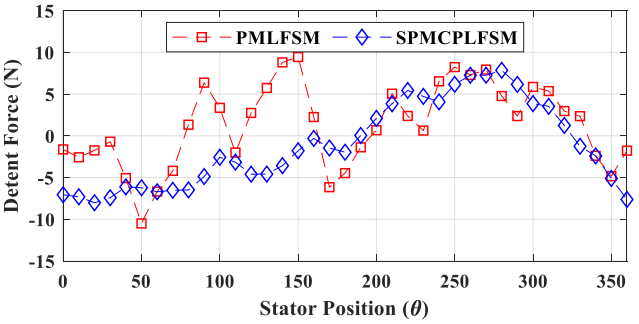

FIGURE 9. Detent force variation between PMLFSM and SPMCPLFSM.

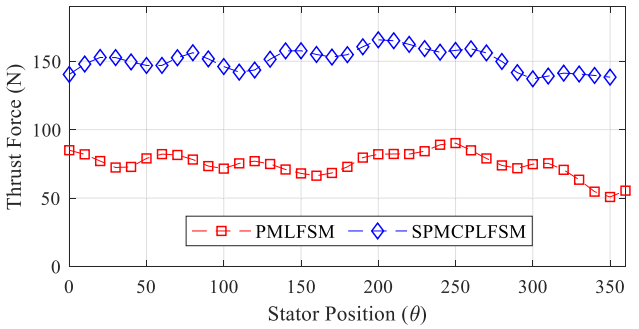

FIGURE 10. Analysis of the thrust force for PMLFSM and SPMCPLFSM.

peak 1.7888 Wb), the positive peak of the PMLFSM is at 0.8648 Wb and the negative peak is at −0.6893 Wb (peak to peak 1. 5541 Wb). It's important to note that SPMCPLFSM achieves symmetric flux linkage as well as 0.2347 Wb improvement in peak-to-peak values despite a 25% decrease in PMs volume.

Figure 9 compares and illustrates the detent force between the proposed SPMCPLFSM and the existing PMLFSM. The SPMCPLFSM design obviously has a smaller peak to peak detent force than the PMLFSM. Peak to peak detent forces for PMLFSM and SPMCPLFSM are 19.9431 N and 15.8647 N, respectively. As a result, the suggested SPMCPLFSM displays less noise and vibration than the PMLFSM because of improved flux modulation that lessens the impacts of slotting.

In Figure. 10, the thrust forces of the PMLFSM and SPMCPLFSM have been displayed and compared. According to analysis, SPMCPLFSM offers thrust force that is both larger in magnitude and less pulsating than PMLFSM. While

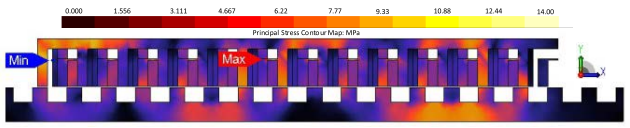

FIGURE 11. Nephogram of principal stress distribution at rated velocity of 171.5 m/sec.

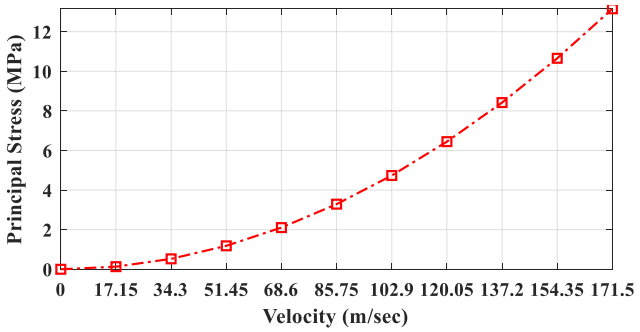

FIGURE 12. Variation of mover principal stress with velocity

SPMCPLFSM has a thrust force of 154.6747 N, PMLFSM exhibits an average thrust force of 76.98461 N. As a result, SPMCPLFSM has more thrust force than the typical PMLFSM and is thought to be suitable for roller coaster applications.

Since proposed SPMCPLFSM model is composed of thin flux bridge therefore to ensure safe operation, mechanical integrity of mover structure is investigated by static structural analysis. In this analysis, constraints are set on flux barrier, flux bridge, mover slot and yoke whereas principal stress is investigated and its Nephogram map under rated velocity as shown in Figure. 11. It can be clearly seen that maximum possible stress up to rated velocity of 171.5 m/sec are 13.156 MPa whereas 35H210 steel sheet have maximum allowable stress of 310 MPa which confirm safe operation of the mover structure. Furthermore, variation of principal stress with various velocities are shown in Figure. 12.

Whereas quantitative electromagnetic performance between PMLFSM and SPMCPLFSM are listed in Table 4. Analysis shows that SPMCPLFSM enhance Φ_{p-p} by 15.10%, suppress F_d by 20.41%, boost T_F to 2 times, diminish T_{F-rip} by 27.68%, curtailed K_{rip} by 1.77 times and boost T_{F-den} to 2.64 times. Furthermore, V_{PM} is reduced to 25% which reduces total PM weight and overall PM cost by 24.16%.

In order to further evaluate effectiveness of the proposed SPMCPLFSM, the model is compared with LPMSM as shown in Figure. 13 and corresponding electromagnetic performance are listed in Table 5. Analysis shows that SPMCPLFSM enhance Φ_{p-p} by 47.22%, suppress F_d by 26.35%, increased T_F by 45.26%, diminish T_{F-rip} by 18.90%, curtailed K_{rip} by 44.18%.

Thus, it is noted that SPMCPLFSM offers improved performance, according to FEA, which is based on the depiction of key performance metrics. However, FEA requires costly software and gear, is computationally demanding, and takes a

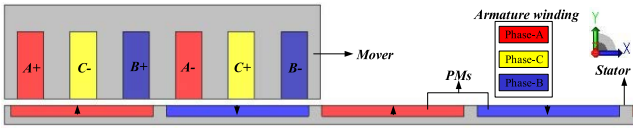

FIGURE 13. Cross sectional view of LPMSM.

TABLE 4. Quantitative electromagnetic performance of PMLFSM and SPMCPLFSM.

Key performance indicator (unit)	PMLFSM	SPMCPLFSM
Φ_{p-p} (Wb)	1.5541	1.7888
F_d (N)	19.9341	15.8647
T_F (N)	76.9846	154.6747
T_{F-rip} (N)	39.428	28.5131
K_{rip} (%)	51.21	18.43
T_{F-den} (kN/m^3)	101.83	269.20
V_{PM} (mm^3)	756000	574560
PM weight (kg)	5.67	4.3
PM cost ($)	737.1	559

TABLE 5. Quantitative electromagnetic performance of LPMSM.

Performance indicator (unit)	LPMSM	SPMCPLFSM
Φ_{p-p} (Wb)	1.215	1.7888
F_d (N)	21.543	15.8647
T_F (N)	106.476	154.6747
T_{F-rip} (N)	35.159	28.5131
K_{rip} (%)	33.020	18.43

lot of time. Therefore, for the initial design of SPMCPLFSM, other analytical modelling methodologies are offered.

IV. ANALYSIS ANALYTICAL MODELLING OF SPMCPLFSM

Different analytical techniques, such as the Laplace Equation in terms of vector potential (For validating MFD), the MST Method in the middle of the air-gap, and the LPMEC (For validating Open-Circuit Flux Linkage), are used to forecast the electromagnetic performance of the SPMCPLFSM (For validation of Detent Force and Thrust force).

A. LPMEC

In terms of the permeance of each machine component, LPMEC models the entire machine. Permeance is used to represent the stator and mover core, whereas series permeance is used to simulate the PMs as MMF sources. Through an air gap, the flux in the SPMCPLFSM alternates between the stator and mover. In the mover yoke, mover tooth, flux bridge, air gap, stator tooth, and stator yoke, the main flux flow is present. Permeance forming LPMEC represents the major flux path. Figure. 14 depicts the LPMEC of the unit section of the SPMCPLFSM.

Various LPMEC module portions have different permeance calculations. It is simple to compute because the MEC modules for the stator and mover stay the same and depend on the same dimensions. Permeance of stator tooth (P_{si}) and stator yoke (P_{st}) are stated as [12].

$$P_{si} = \frac{\mu_0 \mu_r h_{sy} L}{\tau_s + h_{sy}} \tag{4}$$

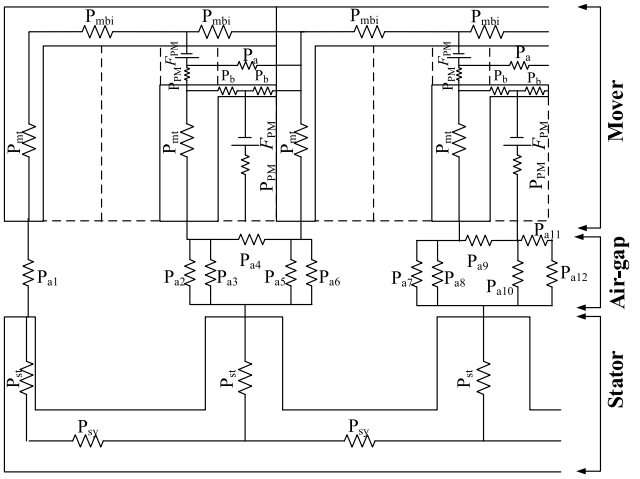

FIGURE 14. LPMEC of the unit section of CPLPMFSM.

$$P_{st} = \frac{\mu_0 \mu_r w_{st} L}{w_{st}} \tag{5}$$

The mover's MEC module is unchanged and dependent on dimension. The computation of the permeance of the mover's teeth and yoke is given in [12].

$$P_{mi} = \frac{\mu_0 \mu_r h_{my} L}{\tau_m + h_{my}} \tag{6}$$

$$P_{mt} = \frac{\mu_0 \mu_r w_{mt} L}{w_{mt}} \tag{7}$$

PMs are modeled by MMF sources with series permeance in the LPMEC module. Along with permeance, flux sources may also be used to designate PMs. The flux source (Φ_{PM}) and PMs MMF ($\mathcal{F}_{PM}$) may be computed as.

$$\mathcal{F}_{PM} = \frac{B_r . w_{PM}}{\mu_0 \mu_r} \tag{8}$$

$$\Phi_{PM} = B_r . A_{PM} . \tag{9}$$

As the orientation of the mover teeth changes, so does the magnetic flux distribution between the mover and the stator. Changes in the distribution of air-gap flux tubes at certain mechanical degrees lead to changes in the air-gap MEC modules. This article analyses and studies five distinct LPMEC modules at various mechanical phases. The varieties of flux tubes are used to compute the permeance of the MEC module in the unit section of the LPMEC. Figure 15$(a-f)$ depicts six different types of flux tubes as revealed by FEA, and their corresponding permeances are indicated as P_a to P_f [22].

$$P_a = \frac{\theta \mu L}{\ln\left(r_2/r_1\right)} \tag{10}$$

$$P_b = \frac{L\mu}{\theta} \ln\left(r_2/r_1\right) \tag{11}$$

$$P_c = \frac{L\mu}{x} \tag{12}$$

$$P_d = \frac{2L\mu}{\pi} \ln\left(1 + x\pi/r\pi + 2h\right) \tag{13}$$

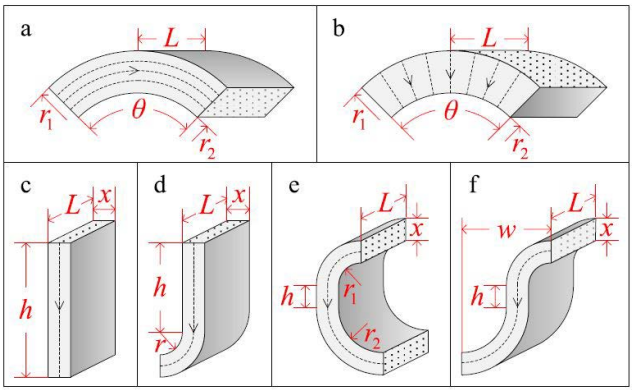

FIGURE 15. Observed flux tubes from FEA.

$$P_e = \frac{L\mu}{\pi} \ln\left(1 + {}^{2x\pi}/_{r_1\pi + r_2\pi + 2h}\right) \tag{14}$$

$$P_f = \frac{2xL\mu}{w\pi + 2h} \tag{15}$$

The incidence matrix (M) of the circuit with node i and branch j is produced using the permeance of each module and the permeance network formed using LPMEC is

$$M_{i,j} = \begin{cases} 0, & nodei\ i\ and branchjisnotconnected. \\ -1, & branch\ j\ terminatetonodei. \\ 1, & branchjstartfromnodei. \end{cases} \tag{16}$$

Kirchhoff Circuit Law may be used to determine Node Magnetic Potential as

$$U = M^t.V \tag{17}$$

$$M.\Phi = 0 \tag{18}$$

$$U = R.\Phi + E = \Lambda^{-1}.\Phi + E \tag{19}$$

where E is the branch MMF source and Λ denotes the permeance matrix. The method for computing node magnetic potentials is [19].

$$V = (M.\Lambda.M^t)^{-1}.(M.\Lambda.E) \tag{20}$$

B. MAGNETIC FLUX DENSITY

By incorporating the carter coefficient, the cartesian coordinated reference system is used to compute MFD components in the middle of the air-gap while taking slotting effects into account [10]. Under no-load and on-load situations, the MFD component (B_x and B_y) of the SPMCPLFSM is analytically derived using LEs [23] in terms of vector potential. Figure 16 illustrates the unit section of the SPMCPLFSM's boundary condition in the xy reference system with respect to the origin.

The middle of the air gap is where MFD start i.e. $y = \delta/2$ is stated as

$$B_o\tau_m = \int B_y\left(x, \delta/2\right) dx \tag{21}$$

MFD's symmetry around the origin necessitates boundary conditions along its vertical sides xy and $x'y'$ as

$$B_x\left(\tau_m/2, y\right) = B_x\left(-\tau_m/2, y\right) = 0 \quad \forall y\epsilon\,[0, \delta] \tag{22}$$

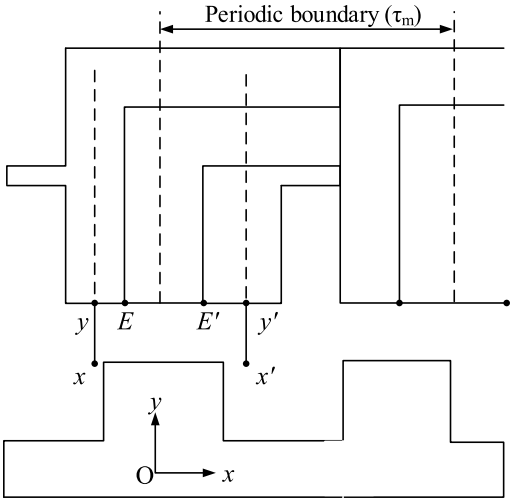

FIGURE 16. Boundary condition in xy reference system.

Because of the assumption that the iron core has infinite permeability, the boundary condition for MFD along xx' is directed in the vertical direction

$$B_x\,(x, 0) = 0 \quad \forall x\epsilon\left[-\tau_m/2, \tau_m/2\right] \tag{23}$$

Similar to this, the MFD across yy' is solely pointed in the y direction.

Over the span $x\epsilon\left[-\tau_m/2, \tau_m/2\right]$, the average MFD meeting the boundary condition is

$$B_o = \frac{1}{\tau_m} \int_{-\tau_m/2}^{\tau_m/2} B_y\,(x, y)\,dx \tag{24}$$

The following summarizes the MFD component as a Fourier series

$$B_{EE'}\,(x) = \sum_{n=1}^{\infty} F_n \sin\left(\frac{2\pi nx}{\tau_m}\right) \tag{25}$$

where, one can calculate the Fourier series coefficient by

$$F_n = \frac{4.c.W_n}{\tau_m} \tag{26}$$

Any positive integer can have the constant term W_n evaluated via an integral numerical solution as shown below.

$$W_n = \int_0^{w_{ms}} \left[\frac{1}{\sqrt[3]{\frac{w_{ms}}{2} - x}} - \frac{1}{\sqrt[3]{\frac{w_{ms}}{2} + x}}\right] \sin\left(\frac{2\pi nx}{\tau_m}\right) \tag{27}$$

While the Carter coefficient (k_c), which is provided by

$$k_c = \frac{B_{max}}{B_o} \tag{28}$$

$$B_{max} = B_o - \sum_{n=1}^{\infty} \frac{2\pi nA_n \cos(\pi n)}{\tau_m} \cosh\left(\frac{\pi ng}{\tau_m}\right) \tag{29}$$

$$B_{max} = B_o - \sum_{n=1}^{\infty} (-1)^n \frac{4\pi n c W_n \cosh\left(\frac{\pi ng}{\tau_m}\right)}{\pi n \tau_m \sinh\left(\frac{2\pi ng}{\tau_m}\right)} \tag{30}$$

$$B_{max} = B_o - \sum_{n=1}^{\infty} \frac{2(-1)^n c W_n}{\tau_m \sinh\left(\frac{\pi ng}{\tau_m}\right)} \tag{31}$$

$$c = \frac{(k_c - 1) B_{avg}}{K} \tag{32}$$

$$K = -\sum_{n=1}^{\infty} \frac{2(-1)^n W_n}{\tau_m \sinh\left(\frac{\pi ng}{\tau_m}\right)} \tag{33}$$

Finally, term 'c' is expressed as

$$c = \frac{(k_c - 1) B_o}{-\sum_{n=1}^{\infty} \frac{2(-1)^n W_n}{\tau_m \sinh\left(\frac{\pi ng}{\tau_m}\right)}} \tag{34}$$

Analytical expression of MFD obtained by vector potential governed by general form of LEs

$$\frac{\partial^2 P}{\partial x^2} + \frac{\partial^2 P}{\partial y^2} = 0 \tag{35}$$

After solving for the appropriate boundary conditions and vector potential, the B_x and B_y MFD components may be expressed as follows

$$B_x(x, y) = \frac{\partial P(x, y)}{\partial y} \tag{36}$$

$$B_y(x, y) = -\frac{\partial P(x, y)}{\partial x} \tag{37}$$

Conveniently, General LE may be expressed in writing as follows

$$P(x, y) = -B_o x + \sum_{n=1}^{\infty} A_n \cosh\left(\frac{2\pi ny}{\tau_m}\right) \sin\left(\frac{2\pi nx}{\tau_m}\right) \tag{38}$$

Constant term (A_n) can be calculated

$$A_n = \frac{2cW_n}{n\pi \sinh(\frac{2\pi gn}{\tau_m})} \tag{39}$$

Using generic LEs to solve for B_x and B_y MFD components

$$B_x(x, y) = \sum_{n=1}^{\infty} \frac{2n\pi A_n}{\tau_m} \sinh\left(\frac{2n\pi y}{\tau_m}\right) \sin\left(\frac{2n\pi x}{\tau_m}\right) \tag{40}$$

$$B_y(x, y) = B_o - \sum_{n=1}^{\infty} \frac{2n\pi A_n}{\tau_m} \cosh\left(\frac{2n\pi y}{\tau_m}\right) \cos\left(\frac{2n\pi x}{\tau_m}\right) \tag{41}$$

Applying boundary condition and substitute A_n finally, B_x and B_y MFD becomes obtained are expressed as

$$B_x(x, y) = \sum_{n=1}^{\infty} \frac{4cW_n \sinh\left(\frac{2n\pi y}{\tau_m}\right) \sin\left(\frac{2n\pi x}{\tau_m}\right)}{\tau_m \sinh\left(\frac{2n\pi g}{\tau_m}\right)} \tag{42}$$

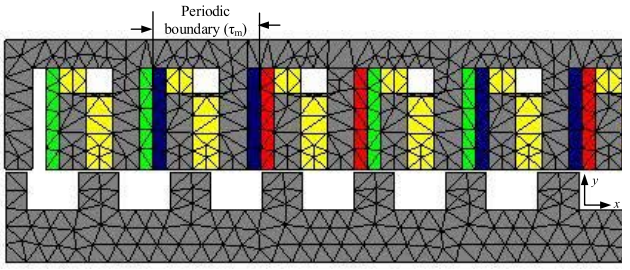

FIGURE 17. Periodic boundary and SPMCPLFSM mesh.

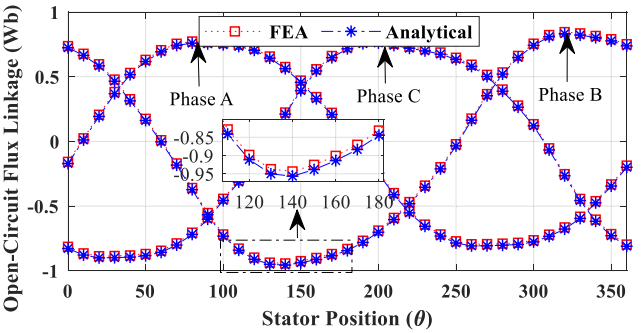

FIGURE 18. Open-circuit flux linkage validation for SPMCPLFSM via analytical model.

$$B_y(x, y) = B_o - \sum_{n=1}^{\infty} \frac{4cW_n \cosh\left(\frac{2n\pi y}{\tau_m}\right) \cos\left(\frac{2n\pi x}{\tau_m}\right)}{\tau_m \cosh\left(\frac{2n\pi g}{\tau_m}\right)} \tag{43}$$

It is worth mentioning that under no-load condition influence of only PM excitation is considered whereas at loaded condition, current density applied to armature winding slots are taken into consideration and can be expressed as [24]

$$J = 0.5(J_{i1} + J_{i2}) + \sum J_{in} \cos\left[\frac{n\pi}{d_{sa}}(\alpha + 0.5d_{sa} - \alpha_i)\right] \tag{44}$$

$$J_{in} = 2/\pi n (J_{i1} - J_{i2}) \sin(0.5\pi n) \tag{45}$$

C. DETENT FORCE

In PMLFSM and SPMCPLFSM, detent force often introduces significant thrust force ripples. End force and slotting effect are the causes of the detent force. Due of the low PM volume, the effects of the detent force in the SPMCPLFSM are less than those in the PMLFSM. In [12], it is describing how to compute the detent force of the CPLPMFSM using the B_x and B_y MFD components.

$$F_d = \frac{GCD(N_{ms}, N_{st}).L}{\mu_o} \int_0^L B_x(x, y).B_y(x, y).dx \tag{46}$$

where N_{ms} is number of mover slots and N_{st} is stator teeth.

D. THRUST FORCE

In the air-gap mid, thrust force of the SPMCPLFSM is obtained using the MST technique using

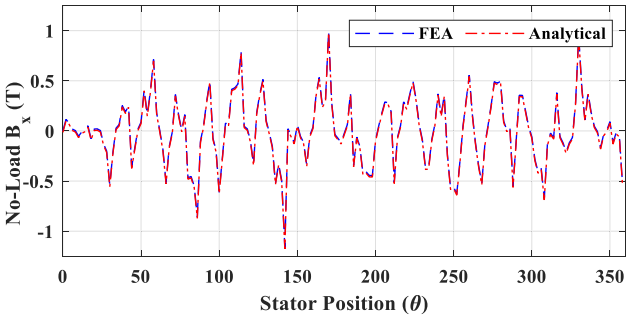

FIGURE 19. No-load B_x MFD component of SPMCPLFSM with FEA and analytical.

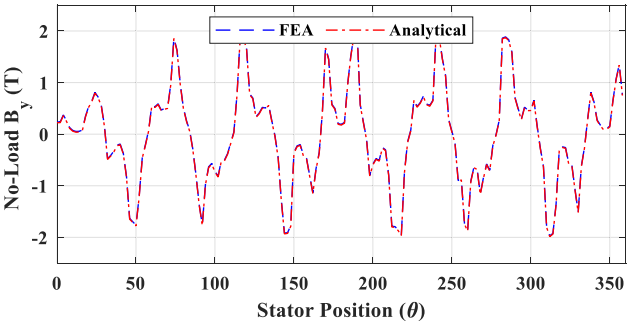

FIGURE 20. No-load B_y MFD component of SPMCPLFSM with FEA and analytical.

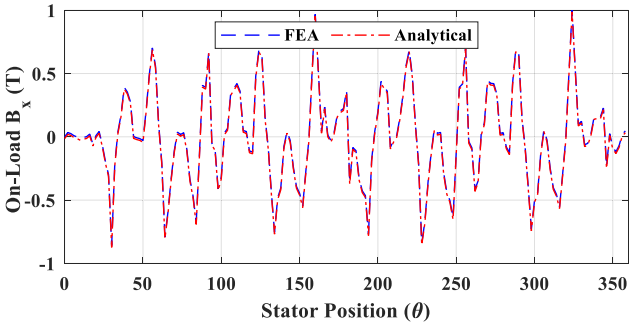

FIGURE 21. On-load B_x MFD component of SPMCPLFSM with FEA and analytical.

MFD components as

$$F_x = \frac{L}{\mu_o} \sum_{n=-\infty}^{\infty} \int_{o}^{\tau_m} \left(B_x\,(x, y)\,.B_y\,(x, y)\right) dx \qquad (47)$$

It should be noted that the computation of thrust force uses the On-load B_x and B_y components of MFD components.

V. VALIDATION OF ANALYTICAL METHODOLOGIES

Using JMAG Commercial FEA Package v. 18.1 with a one mover pole pitch periodic boundary and a 1 mm mesh size as illustrated in Figure. 17, analytical approaches are solved for CPLPMFSM, and the related results produced are compared with current FEA.

The model is validated under no-load with only PM and loaded condition with applied current density of 15A/mm2.

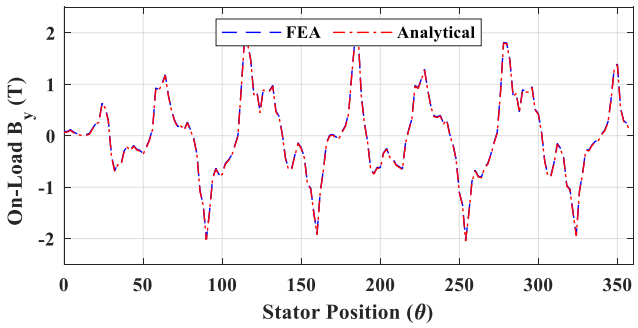

FIGURE 22. On-load B_y MFD component of SPMCPLFSM with FEA and analytical.

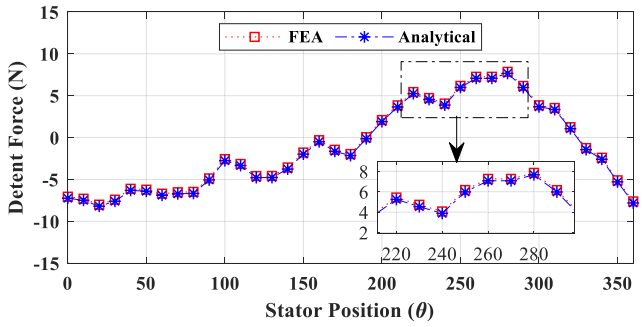

FIGURE 23. Detent force comparison of SPMCPLFSM with FEA and analytical.

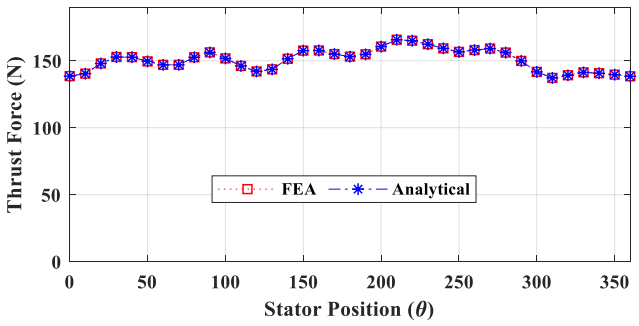

FIGURE 24. Thrust force comparison of SPMCPLFSM with FEA and analytical.

As shown in Figure. 18, the open-circuit flux linkage for the SPMCPLFSM's original design is determined using LPMEC modelling and contrasted with the current FEA. Analysis shows that the associated FEA fairly matches the projected analytical modelling, with a peak error of 1.85%.

Using LEs in terms of vector potential at the middle of the air-gap, the B_x and B_y MFD components of the SPMC-PLFSM were predicted under no-load and on-load situations. Figures 19 and 20 compare the no-load B_x and B_y MFD components to the corresponding FEA, whereas Figures 21 and 22 compare the B_x and B_y MFD components to the corresponding FEA under load circumstances. In accordance with widely established FEA, analysis shows that the accuracy of the expected analytical modelling of the no-load B_x and B_y MFD components for the first design of CPLPMFSM is around 98%.

TABLE 6. Comparative analysis of electromagnetic performance for design of SPMCPLFSM.

Key performance indicator (unit)	2D-FEA	3D-FEA	Analytical
Φ_{p-p} (Wb)	1.7888	1.7641	1.7765
F_d (N)	15.8647	15.5431	15.6941
T_F (N)	154.6747	154.4682	154.5192
T_{F-rip} (N)	28.5131	28.2598	28.3518
K_{rip} (%)	18.43	18.35	18.38
T_{F-den} (kN/m^3)	269.20	268.52	269.00

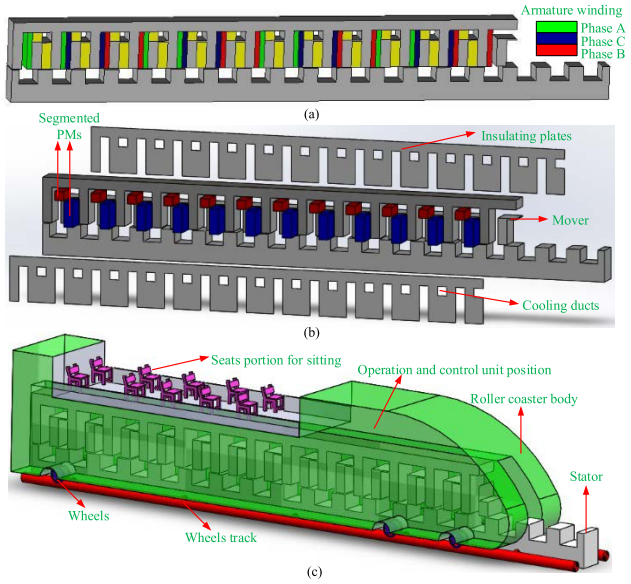

FIGURE 25. Cross sectional view of (a) 3D design (b) Exploded view of manufacturing process and (c) 3D CAD model of the final design prototype.

As illustrated in Figure 23, the detent force in SPMCPLFSM is computed using MST and verified with FEA using the no load B_x and B_y MFD components. According to analysis, the initial design of the SPMCPLFSM's analytically projected detent force indicates an inaccuracy of 2% when compared to the equivalent FEA. Note that the mean value for detent force is -1.008 N and not a null-mean due to dominant attraction force in the y-direction which can be easily compensated through optimization and by converting the design to dual mover and dual stator structure to balance attractive forces.

To compute the thrust force in the SPMCPLFSM using MST and compare it to FEA, on-load B_x and B_y MFD components is employed. According to analysis, FEA results for the expected analytical modelling of thrust force for the basic design of SPMCPLFSM with 2.2% error.

Finally, to justify 2-D FEA and analytical methodologies, 3D- FEA based electromagnetic performance analysis is carried out for precise analysis. Detailed comparison of the 2D/3D and analytical methodology is listed in table 6 whereas 3D cross sectional view, exploded view of manufacturing process and its application as roller coaster is shown in Figure. 25. From table 6, it can be clearly seen that both 2D and analytical results fairly match with corresponding 3D FEA. It is worth noting that since the developed model is in initial stage therefore, a comprehensive experimental validation will be presented after design optimization in the future.

VI. CONCLUSION

In this paper a novel high thrust force density SPMCPLFSM with flux bridges and flux barrier are proposed for roller coaster application. In comparison with conventional PMLFSM, the proposed SPMCPLFSM diminish detent force by 20.41%, suppress thrust force ripples by 27.68%, reduces ripple ratio by 1.77 times, improve thrust force to 2 times and boost thrust force density to 2.64 times utilizing 75% of the total PM volume that reduces PM cost by 24.16%. Moreover, flux leakage in PMLFSM are successfully overcomes through flux bridges in SPMCPLFSM. Furthermore, computational complexity, computation time and drive storage and overcome utilizing alternate analytical model. The analytical model is verified using the JMAG Commercial FEA Package version 18.1 and exhibits good agreement with an accuracy of about ∼97%. As a result, authors are confident to suggest proposed SPMCPLFSM for roller coaster application and analytical models for initial design purpose.

REFERENCES

[1] R. Cao, M. Cheng, C. C. Mi, and W. Hua, "Influence of leading design parameters on the force performance of a complementary and modular linear flux-switching permanent-magnet motor," *IEEE Trans. Ind. Electron.*, vol. 61, no. 5, pp. 2165–2175, May 2014.

[2] K. T. Chau, C. C. Chan, and C. Liu, "Overview of permanent-magnet brushless drives for electric and hybrid electric vehicles," *IEEE Trans. Ind. Electron.*, vol. 55, no. 6, pp. 2246–2257, Jun. 2008.

[3] C. F. Wang, J. X. Shen, Y. Wang, L. L. Wang, and M. J. Jin, "A new method for reduction of detent force in permanent magnet flux-switching linear motors," *IEEE Trans. Magn.*, vol. 45, no. 6, pp. 2843–2846, Jun. 2009.

[4] J. Ou, Y. Liu, M. Schiefer, and M. Doppelbauer, "A novel PM-free high-speed linear machine with amorphous primary core," *IEEE Trans. Magn.*, vol. 53, no. 11, pp. 1–8, Nov. 2017.

[5] C.-C. Hwang, P.-L. Li, and C.-T. Liu, "Design and analysis of a novel hybrid excited linear flux switching permanent magnet motor," *IEEE Trans. Magn.*, vol. 48, no. 11, pp. 2969–2972, Nov. 2012.

[6] W. Zhao, M. Cheng, J. Ji, R. Cao, Y. Du, and F. Li, "Design and analysis of a new fault-tolerant linear permanent-magnet motor for maglev transportation applications," *IEEE Trans. Appl. Supercond.*, vol. 22, no. 3, Jun. 2012, Art. no. 5200204.

[7] R. Cao, M. Cheng, C. Mi, W. Hua, X. Wang, and W. Zhao, "Modeling of a complementary and modular linear flux-switching permanent magnet motor for urban rail transit applications," *IEEE Trans. Energy Convers.*, vol. 27, no. 2, pp. 489–497, Jun. 2012.

[8] Y. Du and N. Jin, "Research on characteristics of single-sided linear induction motors for urban transit," in *Proc. Int. Conf. Electr. Mach. Syst.*, Tokyo, Japan, Nov. 2009, pp. 1–4.

[9] L. Huang, H. Yu, M. Hu, and H. Liu, "Study on a long primary flux-switching permanent magnet linear motor for electromagnetic launch systems," in *Proc. 16th 17th Int. Symp. Electromagn. Launch Technol.*, Beijing, China, May 2012, pp. 1–6.

[10] J.-A. Duan, H.-B. Zhou, and N.-P. Guo, "Electromagnetic design of a novel linear maglev transportation platform with finite-element analysis," *IEEE Trans. Magn.*, vol. 47, no. 1, pp. 260–263, Jan. 2011.

[11] N. Hodgins, O. Keysan, A. S. McDonald, and M. A. Mueller, "Design and testing of a linear generator for wave-energy applications," *IEEE Trans. Ind. Electron.*, vol. 59, no. 5, pp. 2094–2103, May 2012.

[12] N. Ullah, M. K. Khan, F. Khan, A. Basit, W. Ullah, T. Ahmad, and N. Ahmad, "Comparison of analytical methodologies for analysis of single sided linear permanent magnet flux switching machine: No-load operation," *Appl. Comput. Electromagn. Soc.*, vol. 33, no. 8, pp. 923–930, 2018.

[13] Y. Gao, D. Li, R. Qu, H. Fang, H. Ding, and L. Jing, "Analysis of a novel consequent-pole flux switching permanent magnet machine with flux bridges in stator core," *IEEE Trans. Energy Convers.*, vol. 33, no. 4, pp. 2153–2162, Dec. 2018.

[14] Z. Liang, Y. Gao, D. Li, and R. Qu, "Design of a novel dual flux modulation machine with consequent-pole spoke-array permanent magnets in both stator and rotor," *CES Trans. Electr. Mach. Syst.*, vol. 2, no. 1, pp. 73–81, Mar. 2018.

[15] I. Eguren, G. Almandoz, A. Egea, G. Ugalde, and A. J. Escalada, "Linear machines for long stroke applications—A review," *IEEE Access*, vol. 8, pp. 3960–3979, 2020.

[16] N. Ullah, A. Basit, F. Khan, Y. A. Shah, A. Khan, O. Waheed, and A. Usman, "Design and optimization of complementary field excited linear flux switching machine with unequal primary tooth width and segmented secondary," *IEEE Access*, vol. 7, pp. 106359–106371, 2019.

[17] S. Hussain, F. Khan, W. Ullah, B. Ullah, and B. Khan, "Development of a low-cost modular structure fault tolerant field excited flux switching linear machine for urban rail transit," *IEEE Access*, vol. 9, pp. 165854–165864, 2021.

[18] B. Ullah, F. Khan, S. Hussain, and B. Khan, "Modeling, optimization, and analysis of segmented stator flux switching linear hybrid excited machine for electric power train," *IEEE Trans. Transport. Electrific.*, vol. 8, no. 3, pp. 3546–3553, Sep. 2022.

[19] N. Ullah, F. Khan, W. Ullah, M. Umair, and Z. Khattak, "Magnetic equivalent circuit models using global reluctance networks methodology for design of permanent magnet flux switching machine," in *Proc. 15th Int. Bhurban Conf. Appl. Sci. Technol. (IBCAST)*, Islamabad, Pakistan, Jan. 2018, pp. 397–404.

[20] B. L. J. Gysen, E. Ilhan, K. J. Meessen, J. J. H. Paulides, and E. A. Lomonova, "Modeling of flux switching permanent magnet machines with Fourier analysis," *IEEE Trans. Magn.*, vol. 46, no. 6, pp. 1499–1502, Jun. 2010.

[21] N. Ullah, F. Khan, W. Ullah, A. Basit, M. Umair, and Z. Khattak, "Analytical modelling of open-circuit flux linkage, cogging torque and electromagnetic torque for design of switched flux permanent magnet machine," *J. Magn.*, vol. 23, no. 2, pp. 253–266, Jun. 2018.

[22] V. Ostovic, *Dynamics of Saturated Electric Machines*. Berlin, Germany: Springer-Verlag, 1989.

[23] A. Tessarolo and M. Olivo, "A new method for the analytical determination of the complex relative permeance function in linear electric machines with slotted air gap," in *Proc. Int. Symp. Power Electron., Electr. Drives, Autom. Motion (SPEEDAM)*, Anacapri, Italy, Jun. 2016, pp. 1330–1335.

[24] L. J. Wu, Z. Q. Zhu, D. Staton, M. Popescu, and D. Hawkins, "Analytical modeling of eddy current loss in retaining sleeve of surface-mounted PM machines accounting for influence of slot opening," in *Proc. IEEE Int. Symp. Ind. Electron.*, Hangzhou, China, May 2012, pp. 611–616.

WASIQ ULLAH (Graduate Student Member, IEEE) was born in Peshawar, Khyber Pakhtunkhwa, Pakistan, in 1995. He received the B.S. and M.S. degrees in electrical (power) engineering from COMSATS University Islamabad (Abbottabad Campus), Abbottabad, Pakistan, in 2018 and 2020, respectively, where he is currently pursuing the Ph.D. degree in electrical (power) engineering.

Since 2018, he has been a Research Associate with the Electric Machine Design Research Laboratory. His research interests include analytical modeling, design analysis and optimization of permanent magnet flux switching machines, linear flux switching machines, hybrid excited flux switching machines, novel consequent pole flux switching machines for high-speed brushless ac applications, and flux switching generators for counter-rotating wind turbines applications.

Mr. Ullah is a member of the IEEE-IES Electrical Machines Technical Committee and a member of the Pakistan Engineering Council. He serves as a Reviewer for the IEEE TRANSACTIONS ON MAGNETICS, IEEE ACCESS, IET journals, MDPI journals, IECON-2022, and 2022 IEEE Energy Conversion Congress and Exposition (ECCE 2022).

FAISAL KHAN (Senior Member, IEEE) was born in Charsadda, Khyber Pakhtunkhwa, Pakistan, in 1986. He received the B.S. degree in electronics engineering and the M.S. degree in electrical engineering from COMSATS University Islamabad (Abbottabad Campus), Pakistan, in 2009 and 2012, respectively, and the Ph.D. degree in electrical engineering from the Universiti Tun Hussein Onn Malaysia, Malaysia, in 2017.

From 2010 to 2012, he was a Lecturer at the University of Engineering & Technology, Abbottabad, Pakistan. Since 2017, he has been an Assistant Professor with the Electrical and Computer Engineering Department, COMSATS University Islamabad (Abbottabad Campus). He is the author of more than 100 publications, one patent, and received multiple research awards. His research interests include design and analysis of flux-switching machines, synchronous machines, and dc machines.

Dr. Khan is a member of the IEEE-IES Electrical Machines Technical Committee and a member of the Pakistan Engineering Council.

SHAHID HUSSAIN (Graduate Student Member, IEEE) was born in Swabi, Khyber Pakhtunkhwa, Pakistan. He received the B.S. degree in electrical (power) engineering from COMSATS University Islamabad, Abbottabad Campus, Abbottabad, Pakistan, in 2019, where he is currently pursuing the M.S. degree in electrical (power) engineering. He has been a Research Assistant with the Electric Machine Design Research Laboratory, since 2020. His research interests include design analysis, optimization and experimental validation of modular and complementary fault tolerant field excited linear flux switching machines for long stroke application. He is a member of the Pakistan Engineering Council.

MUHAMMAD YOUSUF (Graduate Student Member, IEEE) received the B.S. degree in electrical engineering (electronics) from the Federal Urdu University of Arts Science and Technology (FUUAST), Islamabad, Pakistan, in 2015, and the M.S. degree in electrical engineering from COMSATS University Islamabad, Islamabad, in 2019. He is currently pursuing the Ph.D. degree in electrical engineering with COMSATS University Islamabad, (Abbottabad Campus), Abbottabad, Pakistan. His research interests include design, analysis, and optimization of permanent magnet flux switching machines, multi-phase machines, and axial flux permanent magnet machines.

SIDDIQUE AKBAR was born in Khyber Pakhtunkhwa, Pakistan, in 1997. He received the bachelor's degree in electrical (power) engineering from COMSATS University Islamabad, Abbottabad Campus, Pakistan, in 2020, where he is currently pursuing the M.S. degree in electrical engineering. He has been a Research Assistant with the Electric Machine Design Research Laboratory, since 2020. His research interests include analysis, optimization, and experimental validation of actuator and flux switching machines.